ADVANCED FUNCTIONAL MATERIALS
www.afm-journal.de

Spintronic Quantum Phase Transition in a Graphene/$Pb_{0.24}Sn_{0.76}Te$ Heterostructure with Giant Rashba Spin-Orbit Coupling

Jennifer E. DeMell, Ivan Naumov, Gregory M. Stephen, Nicholas A. Blumenschein, Y.-J. Leo Sun, Adrian Fedorko, Jeremy T. Robinson, Paul M. Campbell, Patrick J. Taylor, Don Heiman, Pratibha Dev, Aubrey T. Hanbicki, and Adam L. Friedman**

Mechanical stacking of two dissimilar materials often has surprising consequences for heterostructure behavior. In particular, a 2D electron gas (2DEG) is formed in the heterostructure of the topological crystalline insulator $Pb_{0.24}Sn_{0.76}Te$ and graphene due to contact of a polar with a nonpolar surface and the resulting changes in electronic structure needed to avoid polar catastrophe. The spintronic properties of this heterostructure with non-local spin valve devices are studied. This study observes spin-momentum locking at lower temperatures that transitions to regular spin channel transport only at ≈40 K. Hanle spin precession measurements show a spin relaxation time as high as 2.18 ns. Density functional theory calculations confirm that the spin-momentum locking is due to a giant Rashba effect in the material and that the phase transition is a Lifshitz transition. The theoretically predicted Lifshitz transition is further evident in the phase transition-like behavior in the Landé g-factor and spin relaxation time.

1. Introduction

Of the many extraordinary promises of the 2D materials revolution, perhaps none is as captivating as the idea that materials with widely varying properties can be arbitrarily stacked into heterostructures, regardless of lattice spacing or growth mechanism.[1] With a menu of thousands of 2D materials,[2] designer heterostructures are at hand with such remarkable properties as interlayer excitons in transition metal dichalcogenides[3,4] (TMDs), "magic-angle" superconductivity in graphene and TMDs,[5] and ferromagnetism from non-magnetic constituents.[6] In many of these systems, heterostructures are more than simply the sum of their parts. Rather than each layer in a stack acting as a discrete entity, unique hybridization effects result in emergent phenomena.[7,8] One of the most versatile and useful materials is graphene: like tofu, graphene often acquires the flavor of whatever is placed in its proximity.[9,10]

Perhaps the most compelling application of such heterostructures is in next-generation computing devices.[11–13] Primary among the many looming roadblocks of current computing paradigms are device bottlenecks in both energy expenditure and the physical limitations of the ubiquitous

J. E. DeMell, G. M. Stephen, N. A. Blumenschein, A. T. Hanbicki, A. L. Friedman
Laboratory for Physical Sciences
8050 Greenmead Dr., College Park, MD 20740, USA
E-mail: jdemell@lps.umd.edu; afriedman@lps.umd.edu

I. Naumov, P. Dev
Department of Physics and Astronomy
Howard University
Washington, DC 20059, USA

Y.-J. L. Sun
Institute for Research in Electronics and Applied Physics
University of Maryland
College Park, MD 20740, USA

The ORCID identification number(s) for the author(s) of this article can be found under https://doi.org/10.1002/adfm.202311875

DOI: 10.1002/adfm.202311875

A. Fedorko, D. Heiman
Dana Research Center
Northeastern University
Boston, MA 02115, USA

J. T. Robinson, P. M. Campbell
Electronics Science and Technology Division
Naval Research Laboratory
Washington, DC 20375, USA

P. J. Taylor
Army Research Laboratory
2800 Powder Mill Rd., Adelphi, MD 20783, USA

D. Heiman
Plasma Science and Fusion Center
MIT
Cambridge, MA 02139, USA

charge-based CMOS structures.[14] Spin-based "spintronic" devices offer considerably lower energy operation, higher speeds, and greater densities.[15] Because the spin diffusion length is proportional to mobility, a nearly defect-free graphene would seem like an ideal spintronic channel.[16] However, its lack of spin-orbit coupling leaves few options for the spin current control needed for device operation. Combining graphene with a high spin-orbit material such as a topological insulator,[17,18] where the spin-orbit coupling is conveyed by proximity, could be a viable solution.

One recent example of a graphene-based heterostructure with unexpected properties is the graphene/topological crystalline insulator (TCI) system graphene/$Pb_{0.24}Sn_{0.76}Te$ (Gr/PST). While systemic symmetries protect the properties of all topological materials, TCIs are primarily protected by mirror symmetry.[19] Since the TCI has a significantly lower conductivity than graphene, one might expect most of the current to flow through the graphene, resulting in proximitized spin-orbit coupling, similar to other graphene heterostructures.[9,10,20] However, stacking graphene onto the PST breaks the inversion symmetry and destroys the topological state. Due to excess charge, the structure must either change its stoichiometry or undergo a complete charge reconfiguration—a phenomena known as the polar catastrophe. The charge redistribution needed to avoid polar catastrophe results in the formation of a 2D electron gas (2DEG) at the interface, analogous to the interface 2DEG famously discovered in $LaAlO_3/SrTiO_2$ and similar systems.[21] Although the topological order of the PST is destroyed in the heterostructure, electronic structure modifications as a result of electronic reconstruction due to the polar discontinuity at the interface leads to the appearance of a high-mobility 2DEG at the interface. Although this composite may not be a true topological material, it shares many properties with the parent topological PST material, such as high mobility, high spin lifetime, high spin-orbit coupling, and spin-momentum locking.

In this paper, we study the spintronic properties of the 2DEG created at the interface of graphene and PST. We fabricate and measure non-local spin valve (NLSV) devices and discover a low-temperature regime dominated by giant Rashba coupling that enables spin-momentum locking. At higher temperatures, the system transitions to a more typical NLSV device channel, attributable to a Lifshitz transition at ≈40 K. Density functional theory (DFT) analysis is used to understand the spin texture and 2DEG behavior. Our DFT calculations reveal a giant Rashba spin-orbit parameter, along with the Lifshitz transition switching mechanism. We also use the Hanle effect to measure spin lifetimes as a function of temperature. We report spin lifetimes as high as 2.18 ns and spin transport persisting up to at least 500 K, properties highly desirable for spintronics applications. We also compare our measurements here with the charge transport measurements performed previously in this system. The robust spin transport and quantum phase transition in this system could be exploited for future low-power high-performance computing devices.

2. Experimental Section

2.1. Growth Methods

$Pb_{0.24}Sn_{0.76}Te$ (111) (PST) topological crystalline insulator (TCI) films were grown to a thickness of 7 nm on GaAs (001) by molecular beam epitaxy using methods described previously.[21] The stoichiometry was chosen to maximize the bulk bandgap while maintaining the TCI behavior, as discussed in depth elsewhere.[21,22] Graphene was grown by low pressure (5–50 mTorr) chemical vapor deposition on copper foiled at 1030 °C under flowing H_2 and CH_4 gas. After growth, the Cu substrates were etched and transferred to the PbSnTe using a wet process.[23]

2.2. Device Fabrication

To fabricate the NLSV, optical lithography with Shipley S1813 photoresist was first utilized to pattern vias for electrical contacts on the PST followed by electron beam deposition of Ti/Au (5 nm/35 nm) and lift-off in acetone. PST mesas were then defined by a second lithography step followed by ion milling in Ar/H_2 plasma and cleaning in an acetone/ultrasonic bath. A subsequent O_2 plasma descum removed any remaining photoresist residue. Two layers of graphene were then transferred on top of the PST mesas. One layer of graphene creates the graphene/PST heterostructure transport channel, while the second graphene layer is used in a tunnel barrier (TB) contact. Another lithography step using polymethyl methacrylate (PMMA) and deep-UV exposure followed by O_2 plasma shaped the graphene into mesas. PMMA and deep-UV lithography were used here to minimize chemical contamination of the graphene. Semiconductor NLSV devices require a TB to match the conductivities between the metallic spin injection/detection contacts and the semiconductor channel.[24] Devices were fabricated with a TB consisting of fluorographene/MgO. Vias for the TB contacts are defined by optical lithography using Lift Off Resist (LOR5A) and Shipley 1813, particularly designed to minimize residue. The graphene inside the vias was fluorinated by exposure to a XeF_2 gas,[25] which acted to both decouple the two graphene layers and selectively transform the top layer into an insulator. Immediately after fluorination, electron beam deposition is used to deposit MgO/$Ni_{80}Fe_{20}$ (Py)/Au (1.5 nm/30 nm/10 nm). An additional optical lithography/deposition step was performed to define Ti/Au (10 nm/40 nm) top contacts to ensure a good electrical connection. Finally, the devices were fluorinated a second time to ensure that the top layer of graphene was completely insulating. Additional characterization details can be found in the Supporting Information.

2.3. Measurement Methods

NLSV and Hanle effect measurements were performed in a cryogen-free variable temperature cryostat set upon a rotating platform and centered between the poles of a 1 T electromagnet. From previous work on simultaneously fabricated Hall bar devices, measured device mobilities for the heterostructure varied from ≈10000 to 20000 $cm^2\ Vs^{-1}$ with a carrier concentration of $8.0 \times 10^{12}\ cm^{-2}$. Comprehensive charge transport data on the same heterostructures can also be found in the previous work.[21] TB contacts were evaluated using the Rowell criteria[25] and found to be of high quality, likely free of pinholes. See Supporting Information for more information. Measurements were performed with DC bias to maximize dynamic range with many measurements averaged together to eliminate noise and spurious signals.

2.4. Theory Methods

Ab-initio calculations of band structure, Fermi surfaces, and Fermi velocities for the simulated heterostructures were performed with the Vienna Ab-initio Simulation Package (VASP).[26,27] The Perdew-Burke-Ernzerh (PBE) generalized gradient approximation (GGA) was adopted to describe the exchange-correlation potential,[28] and the Projected Augmented Wave (PAW) method[29] was used to describe the interaction between the ionic cores and electrons. Structures were relaxed until the difference in total energies between two ionic steps became smaller than 1×10^{-4} eV. The van der Waals interactions between the graphene layer and the underlying thin film were accounted for by the inclusion of the many-body dispersion correction.[30] A $16 \times 16 \times 1$ Monkhorst-Pack **k**-point grid was used for the Brillouin zone sampling of the supercell. The kinetic energy cutoff was set to 400 eV. All calculations included spin-orbit coupling (SOC). PbSnTe was modeled by replacing some of the Sn atoms with Pb atoms. However, SnTe was mainly used to approximate PbSnTe due to the expense of the calculations. Additional details can be found in the Supporting Information or in the previous work in reference 21, where it was demonstrated that SnTe, PbTe, and PbSnTe all behave similarly in this context, where the dominant heterostructure behavior was from a meeting of polar and non-polar surfaces.

2.5. Non-Local Spin Valve Measurements

To measure the spintronic behavior of the Gr/PST system, we processed the heterostructures into standard NLSV devices (see methods above). **Figure** 1a shows an optical image of a measured Gr/PST spin valve and Figure 1b shows a device schematic. A charge current was applied between one outer non-magnetic reference Ti/Au contact and the adjacent inner TB/ferromagnetic (FM) contact (injection), while monitoring the voltage across the other pair of contacts (detection). The spin injection/detection TB/FM contacts were different widths to exploit magnetic shape anisotropy. A spin-polarized charge current was injected from the FM, across the TB contact, and into the heterostructure 2DEG channel. While charge current only flows along the source-drain path, spins simultaneously diffuse in all directions. The pure spin current at the detector contact results in a spin-splitting of the chemical potential that manifests as a measurable voltage.

Measurement of a NLSV is essential to demonstrating spin current generation and manipulation. **Figure** 2 is a summary of the NLSV measurements at various bias and temperature conditions. A sweeping magnetic field, applied along the easy axis of the FM contacts (Figure 2a, inset), switches the relative orientations of the FM magnetization at their respective coercive fields. This results in a lower (higher) measured voltage when the contacts are parallel (antiparallel). Room temperature NLSV behavior is shown in Figure 2a. The red (blue) curves are for positive (negative) magnetic field sweep directions, and the solid (dotted) lines show data acquired while applying a bias current of +10 μA (-10 μA), accounting for both spin extraction and injection. This was typical behavior for a NLSV with the difference in peak position coming from the difference in switching field of the injection/detection contacts.

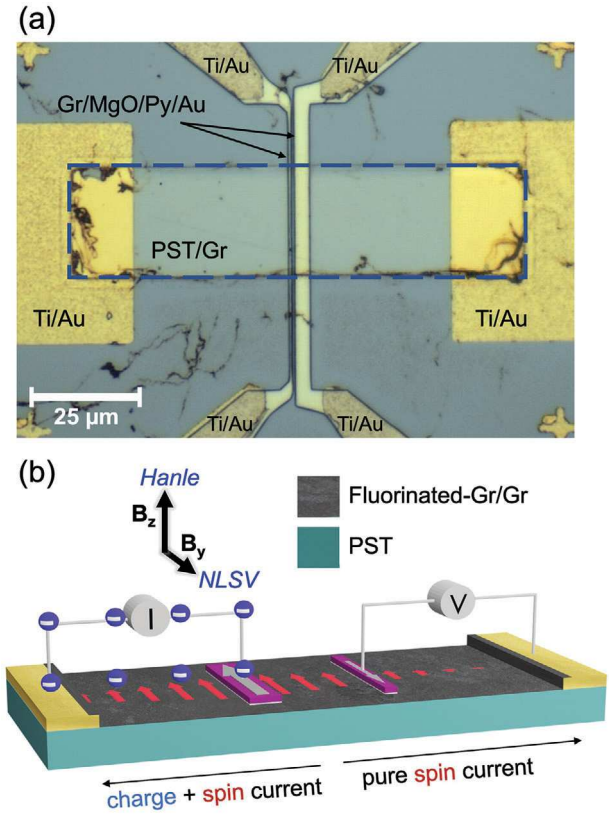

Figure 1. Device image and operation scheme. a) Optical image of the Gr/PST NLSV. Annotations indicate the materials used. For this device, the left and right graphene/MgO/Py/Au TB contacts are 3 and 0.5 μm wide, respectively, and are separated by 1.5 μm. The channel width is 25 μm for all devices measured. b) Device schematic of the NLSV showing operation and externally applied magnetic field. As indicated, the external magnetic field is applied in-plane with the FM contacts for NLSV measurements and out-of-plane with the FM contacts for Hanle effect measurements.

Switching peaks are observed up to 500 K (Figure 2b), the limit of our measurement capabilities, attesting to the robustness of the heterostructure and the device. From the two-wire measurement, bias dependence, and temperature dependence (all shown in further detail in the Supporting Information and in Figure 2c) of the NLSV, we can further confirm that the observed signal is a result of a pure NLSV effect and not anisotropic magnetoresistance.[31–33]

Figure 2c summarizes the temperature dependence of both the non-local resistance ΔR_{NL} and the hysteretic resistance change due to Rashba spin-orbit coupling ΔR_{Rashba}. Hysteresis in the NLSV measurements of a topological or high spin-orbit coupled material is a strong indication of surface state transport. Below 50 K, the NLSV exhibited a strong hysteresis on top of the magnetization switching. This is shown in Figure 2c (inset) with the NLSV data at 3 K. Again, the red (blue) curves are for positive (negative) magnetic field sweeps. The top (bottom) panel was at −0.1 μA (+0.1 μA) bias. A lower bias was used here to emphasize the hysteresis, which also deemphasized the NLSV switching peaks. Therefore, the spin valve peaks were labeled to make the behavior clear. Reversing the bias direction, and also the electrons' momentum, reverses the sign of the

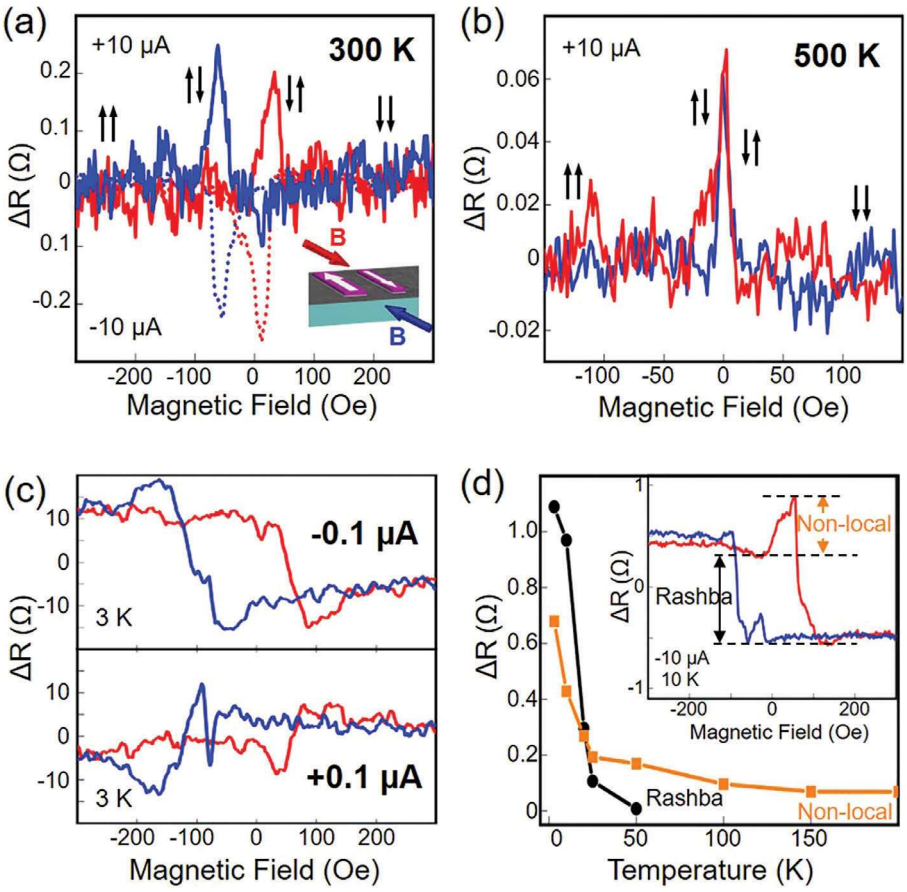

Figure 2. NLSV device operation. Red (blue) lines are for magnetic field sweeping negative to positive (positive to negative). A constant background resistance is subtracted for all plots. a) Non-local resistance versus magnetic field at 300 K for +/−10 μA. Inset shows a device schematic with a sweeping in-plane magnetic field. b) Non-local resistance versus magnetic field at 500 K for +10 μA, demonstrating operation of the spin valve up to high temperature and the limits of our measurement equipment. c) Non-local resistance of the spin injection/extraction switching peak and Rashba hysteretic resistance change as functions of temperature. The inset shows the non-local resistance versus magnetic field for +/−0.1 μA at 3 K showing a switch in the sign of the hysteresis with bias polarity. Arrows indicate the direction of the relative magnetic orientations of the spin valve contacts and the position of the antiparallel switch. d) Total non-local resistance in the spin valve versus magnetic field at 10 K and with a −10 μA bias and defines the relevant system resistances (non-local and hysteretic resistance change due to Rashba spin-orbit coupling) for analysis.

hysteresis. Similar hysteresis was also observed in both topological materials[34] and in 2DEGs[35] as a result of spin-momentum locking, though the origins of the effect for each channel type is different. For a topological material, there is a linear energy dispersion caused by band inversion where each massless, chiral Fermion has its momentum locked at a right angle to a spin-state that is thus protected by symmetry from backscattering. The previous theory work on the Gr/PST heterostructure demonstrated that time reversal symmetry is broken here, resulting in the destruction of the topological state in the PST.[21] For a trivial 2DEG with parabolic energy dispersion, spin-momentum locking, a manifestation of spontaneous nonequilibrium spin polarization caused by an electric current, arises due to Rashba spin-orbit coupling (SOC).[36,37] This is the same effect that allows a measure of control over spin relaxation using an electric field because the spin-splitting energy is proportional to the expectation value of electric field.[38]

Figure 2d shows a magnetic field sweep at 10 K, with the relevant resistances defined in the annotation. ΔR_{Rashba} decreases quickly for increasing temperature until the spin-momentum locking disappears above 40 K. ΔR_{NL} also rapidly decreased with increasing temperature until equilibrating at ≈150 K, where it remained up to at least 500 K (see the Supporting Information for more details). Based on these findings, as well as the DFT calculations presented below, we posit that a Lifshitz phase change occurs at ≈40 K. This conclusion is further supported by previous measurements using only charge transport in this heterostructure.[21] In the Supporting Information, other mechanisms were ruled out including a switch from ballistic-to-diffusive transport and simple thermal effects on the transport.

2.6. Band Structure Calculations

As the temperature is changed, both the Fermi level and the lattice parameter can also change slightly, driving the Lifshitz transition. **Figure 3** shows the calculated band structure for a

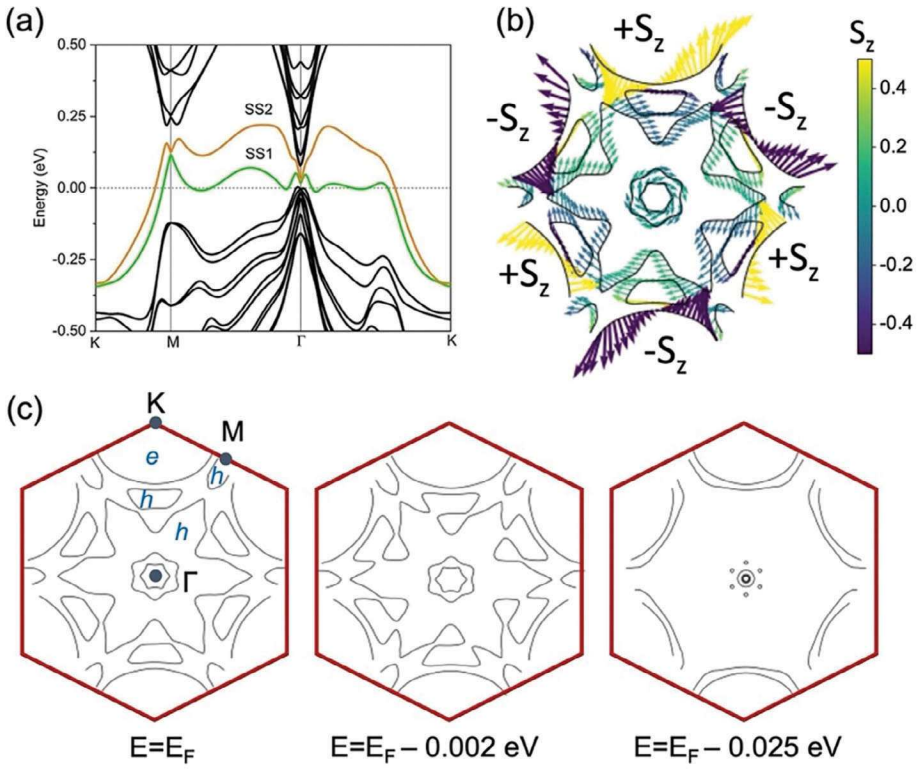

Figure 3. a) Calculated band structure along the high symmetry lines for the heterostructure. Shown in orange (SS1) and green (SS2) are the two surface bands crossing the Fermi level. b) The Fermi surfaces corresponding to the band structure presented in (a), including spin texture. c) Constant energy contours for the energies below the Fermi level corresponding to the band structure presented in (a). Electron and hole pockets are noted by *e* and *h*, respectively.

graphene/SnTe (111) interface. From the SnTe component, this system is expected to inherit topological Dirac points, which are located at the Γ- and M-points.[39] Two additional Dirac points at the Γ-point are inherited from the graphene layer. This is a consequence of zone-folding, with both the K and K' points of graphene folded to the Γ-point in the Brillouin zone of the heterostructure. As shown in Figure 3a, all the Dirac cones at the Γ- and M-points are gapped due to lowering of symmetry in the heterostructure. In the presence of graphene, the C_{3v} point symmetry of SnTe is reduced to C_3-symmetry, which removes the topological protection of the surface states associated with SnTe, opening the gap. Meanwhile, the SnTe film breaks the sublattice symmetry in graphene, opening gaps in the Dirac cones associated with graphene at Γ.

The main feature of the band structure in Figure 3a is the presence of two surface bands crossing the Fermi level. These bands are labeled SS1 (green) and SS2 (orange). Both SS1 and SS2 are mainly localized on the upper graphene side and are characterized by both positive and negative effective masses, depending on **k**. Near the Γ point, these surface bands hybridize with the carbon p_z orbitals. To estimate the strength of the Rashba effect in the heterostructure, the Rashba model was used, in which the SOC splits the parabolic band by shifting the carriers with opposite spin by the momentum $\mathbf{k}_R$. In this model, the SOC coupling parameter, α_R, is defined as $\alpha_R = 2E_R/k_R$, where E_R is the energy difference between the crossing point and the band top or bottom at a particular k_R. Near the M point, along M-Γ for the SS1 band, we find that $k_R \approx 0.18$ Å^{-1} and $E_R \approx 0.13$ eV. This gives $\alpha_R \approx 1.5$ eV Å, which is a giant value for the Rashba parameter. For comparison, it is about half of the largest published value for the Rashba parameter in the literature for BiTeI.[40] The average Fermi velocity was also high (1.5×10^5 m s^{-1}), being ≈30% of the Fermi velocity of Bi_2Se_3.[41]

In Figure 3b, the spin-resolved Fermi surfaces (FSs) are plotted at the Fermi level $E = E_F$. The magnitude of the in-plane component of spin is represented by the length of the arrows, and the color of the arrows gives the *z*-components of the spins. Except for the K-centered FSs, all other FSs had a small S_z component and exhibit Rashba-type spin texture, with the spin being perpendicular to the **k**-vector. In contrast, the K-centered ellipses have a significant S_z component. Moreover, their in-plane spin component tends to be parallel or antiparallel to **k**. Because of their large areas, the electron ellipse around K and the hole star around Γ should produce the dominant contribution to the electric current induced by an applied electric field. The Supporting Information includes calculations for the case when some of the atoms were replaced by Pb, as was the case for the exact structure.

A cross-section of the band structure at various energies below the Fermi level are plotted in Figure 3c. Additional band structure cross-sections and those above the Fermi level are found in the Supporting Information. There are multiple Fermi level crossings at different **k**-points, resulting in many FSs. The large electron ellipse around K, denoted by *e* in Figure 3c, comes from the SS2 band. There are three hole FSs, denoted by *h* in Figure 3c, including a very large star centered on Γ, all related to the SS1

band. There are also two hexagonal FSs around Γ, which are derived from graphene states.

The properties of the surface states SS1 and SS2 play an important role in the generation and registration of spin-polarized currents in the heterostructure. In our experiments, the NLSV device geometry was most sensitive to in-plane spins with Rashba-type spin-momentum locking. As the electronic pockets centered on K (associated with SS2) had high values of out-of-plane spin component S_z, while their in-plane spin texture was not Rashba-like in character, the current-induced spin polarization associated with SS2 is unlikely to be detected. Hence, experimentally, the role of the SS1 states is more important. The SS1 band exhibits Rashba-type spin texture, where the spin lies mostly in-plane, perpendicular to the **k**-vector. A peculiarity of the SS1 band is that it is flat in a wide region of **k**-space close to the Fermi level. As seen in Figure 3c, the SS1 FS changes rapidly for small excursions away from E_F. As a result, the FSs associated with this band can easily adjust their area, shape, and topology under the influence of external parameters such as pressure, composition, temperature, magnetic field, and so on. Abrupt modification of the topology of a Fermi surface is the hallmark of a Lifshitz transition. Therefore, we expect external stimuli such as temperature to strongly affect transport phenomena. For example, a large enhancement of thermoelectric efficiency in SnSe over a wide temperature range (10–300 K) was attributed to the pressure-induced Lifshitz transition.[42] Therefore, our calculations suggest that the system is on the verge of different Lifshitz transitions, which can easily occur under different stimuli, such as Pb-doping, Fermi level tuning, and lattice expansion (for example, through temperature modulation).

The number and complexities of FSs indicate that the experimentally observed disappearance of spin-momentum locking for temperatures above ≈40 K can be ascribed to one or more effects. One such effect is simply the disappearance of some of the hole FSs, which, as discussed, have significant contributions to the spin-polarized current. Another effect is due to high anisotropy of the FSs: a measured change in resistivity, ΔR_{Rashba}, should strongly depend on the orientation of the spin-induced current relative to the heterostructure. With increasing temperature, the anisotropy of the Fermi surfaces may change in such a way that the spin transfer by the drift current becomes inefficient. A third possible effect might be related to the charge redistribution between the p_z orbitals of carbon and the p orbitals of Sn and Te. At polar surfaces, the compensating charge density tends to persist and the carbon p_z orbitals can be filled or emptied at the expense of Sn and Te p orbitals.[43] Since the spin splitting of the graphene Dirac cone (whether n- or p- doped) leads to two Fermi surfaces with opposite spin directions at each momentum, the corresponding current-induced spin densities nearly cancel each other, resulting in the observed behavior.

2.7. Spin Properties

Another important consideration for any spintronic device is the spin polarization. In **Figure 4**, the components of spin polarization derived from both the Rashba (black) and standard NLSV (red) channels are plotted. For a full discussion on the analysis

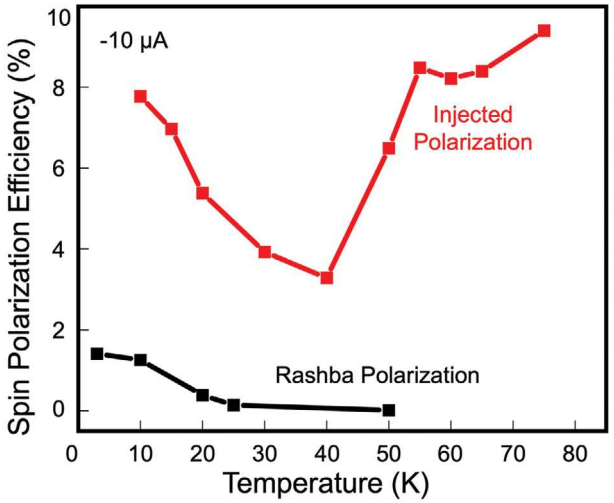

Figure 4. Spin polarization efficiency. Lower bound of the temperature-dependent spin polarization efficiency due to the Rashba spin-momentum locking (red) and of the NLSV (black). Experimental error bars are within the size of the depicted squares at each point.

of each of these components, see the Supporting Information. Comparing the Rashba polarization to the injected polarization, the Rashba component is a significant portion of the observed spin signal at low-temperature before it gradually disappears.

First, we will discuss the low-temperature regime that is dominated by the Rashba effect. Although the origin of spin-momentum locking for topological materials and 2DEGs is different, the theory to analyze the hysteresis is identical.[44] For both topological materials and 2DEGs and for both ballistic and diffusive transport, the high- and low-voltage states in the hysteresis curve are described by[44–47]

$$\Delta R_{Rashba} = \frac{h^2}{e^2} \frac{P_{FM}}{2 v_F W m^*} \left(\mathbf{p}_{\mathbf{Rashba}} \cdot \mathbf{m}_{\mathbf{u}}\right) \quad (1)$$

where h is Planck's constant, e is the elementary charge, P_{FM} is the polarization of the ferromagnetic detector contact (~48% for $Ni_{80}Fe_{20}$),[49] v_F is the Fermi velocity, m^* is the effective mass, W is the width of the channel, $\mathbf{p}_{\mathbf{Rashba}}$ is the induced spin polarization due to the Rashba effect, and $\mathbf{m}_{\mathbf{u}}$ is a unit vector along the direction of magnetization.[21] In previous studies, spontaneous, non-equilibrium spin polarization due to either the Rashba effect or topological surface state spin-momentum locking is distinguishable by having opposite signs in the vector $\mathbf{p}_{\mathbf{Rashba}}$. However, as many others have noted,[34,45,49] it is difficult to draw any conclusions about the sign of the polarization. Therefore, an absolute value of polarization was calculated, displayed versus temperature in Figure 4.

The polarization efficiency, P_{NLSV}, due to injection/extraction into/from a NLSV can be calculated from the injection/extraction NLSV peaks, as defined in Figure 2d. The relationship between the measured resistance and polarization[24] is $\Delta R_{NL} = \frac{P_{NLSV}^2 \lambda_s}{W\sigma} e^{-L/\lambda_s}$. Here, W is the width of the spin channel, σ is the measured temperature-dependent conductivity, and L is the contact spacing. The spin diffusion length $\lambda_s = (D\tau_s)^{1/2}$, where τ_s is the spin lifetime (calculated from fitted Hanle curves below)

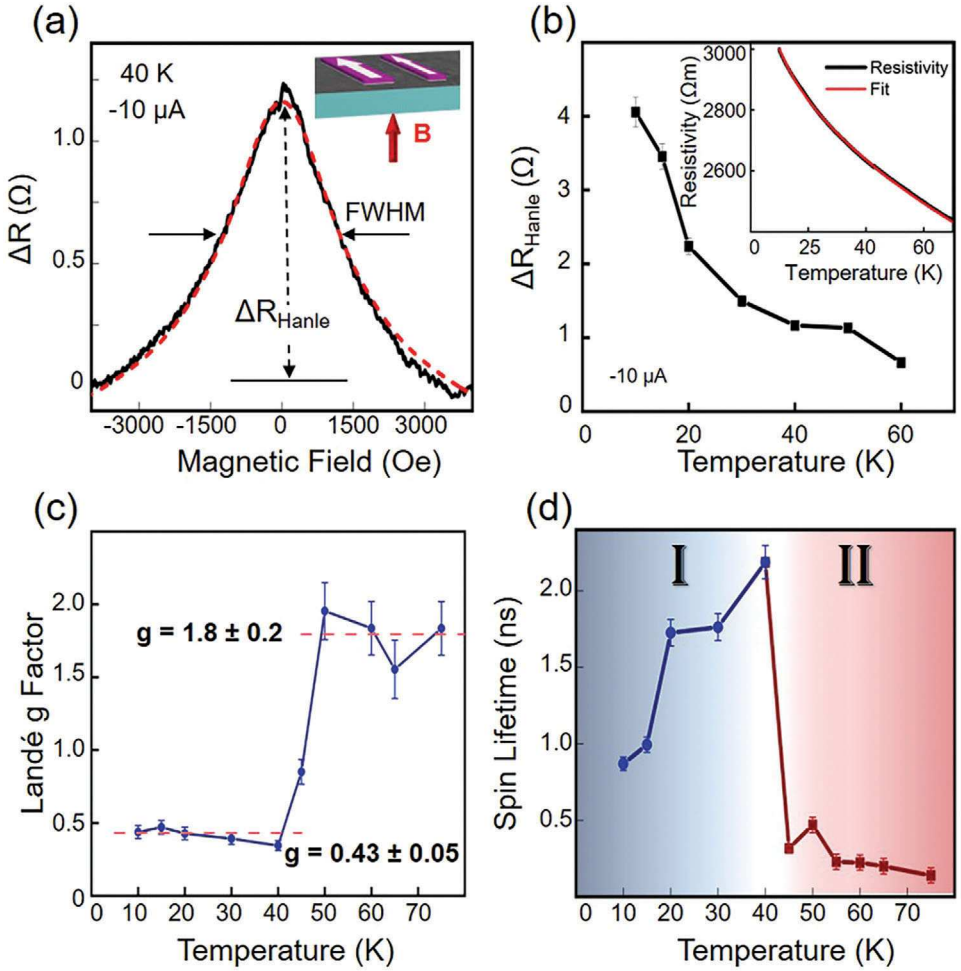

Figure 5. Hanle Effect. a) Non-local resistance versus magnetic field of an example Hanle effect curve showing the expected pseudo-Lorentzian behavior. The red line is a fit to the solution to the spin diffusion equation using the Landé *g* factor and the spin lifetime as fitting parameters at a temperature of 40 K and bias of −10 μA. A background quadratic magnetoresistance was subtracted from the data. b) Non-local resistance versus temperature for the Hanle effect until it disappears at ≈75 K. The inset displays the four-terminal local sheet resistivity versus temperature at a bias of −10 μA, fit to a model that includes variable range hopping, thermal activation, and a linear fit. c) The Landé g-factor as a fitting parameter for the Hanle curves demonstrating an abrupt phase change between 40 and 45 K. d) Temperature dependence of extracted spin lifetime taken at a bias of −10 μA. The two regimes corresponding to Rashba-dominated transport and spin channel-dominated transport are noted as I in blue and II in red.

and D is the spin diffusion constant. Because this system has degeneracies (at least two spin/charge channels), we used the exact solution of the diffusion constant such that[50]

$$D = (k_B T/e)\,(1 + e^{-\eta_f})\ln|1 + e^{\eta_f}| \quad (2)$$

where $\eta_f = E_g/k_B T$, E_g is the system bandgap obtained from DFT calculations as a lower bound on the realistic actual bandgap and k_B is the Boltzmann constant. For an ideal non-degenerate system, Equation (2) reduces to the Einstein relation. The spin diffusion constants calculated from a measurement of mobility in this system at 10 K for PST, graphene, and the heterostructure are 0.172, 3.27, and 17.2 $cm^2\ s^{-1}$, respectively. The shape of the injected polarization in Figure 2d is due to a two-level measured spin relaxation time, discussed below. Comparing the Rashba polarization to the injected polarization, the Rashba component is a significant portion of the observed spin signal at low-temperature before it gradually disappears.

Further spintronic properties of the heterostructure can be extracted from analysis of the Hanle effect, shown in **Figure 5**. Here, a magnetic field is applied out of plane with respect to the moments of the FM injector/detector contacts as is depicted in schematic in Figure 5a. This causes the spins in the channel to precess at the Larmor frequency, $\omega_L = g\mu_B B_z/\hbar$, where g is the Landé g-factor, μ_B is the Bohr magneton, and B_z is the out-of-plane magnetic field. As the magnetic field is increased, precessional dephasing results in a higher resistance, thus a magnetic field sweep will trace out a pseudo-Lorentzian line shape proportional to solutions to the spin diffusion equation described by the steady state spin current[51]

$$S\,(x_1, x_2, B_z) = S_0 \int_0^\infty \frac{1}{\sqrt{4\pi Dt}}\, e^{-(x_2 - x_1 - v_d t)^2/4Dt} \cos(\omega_L t)\, e^{-t/\tau_s} dt \quad (3)$$

where spin is injected into the graphene at x_1 and $t = 0$ and is detected at x_2. S_0 is the spin injection rate and v_d is the electron drift velocity (equal to 0 for pure spin currents). Fits to the Hanle data provide a measure of the spin lifetime. The Landé g-factor for graphene is known to be 2.[52] However, for PST, the Landé g-factor is not accurately known[53] and is unknown for the heterostructure 2DEG because it is difficult to separate bulk and surface g-factors in the heterostructure. Therefore, we leave the Landé g-factor as a fitting parameter.

Figure 5a is a plot of non-local resistance as a function of applied out-of-plane field for a device at a temperature of 40 K. The pseudo-Lorentzian behavior is a signature of the Hanle effect, that is, precessional dephasing of the spin current at the detection contact. The data are in black while the red dashed line shows the fit to Equation (3). A second-order polynomial background was subtracted from the raw Hanle data to remove trivial magnetoresistance. Figure 5b summarizes the change in non-local resistance (ΔR_{Hanle}, as defined in Figure 5a) as a function of temperature. Although the NLSV signal persisted to at least 500 K (Figure 2b), the Hanle signal disappeared above ≈75 K. This behavior was been observed in many previously studied spin valves,[54,55] with the NLSV signal far outlasting the Hanle signal, and was been attributed to thermal fluctuations and phonon scattering.

Insight into the momentum scattering behavior is learned from temperature-dependent resistivity measurements. The inset of Figure 5b shows the four-terminal sheet resistivity (ρ_{Sheet}) versus temperature measured in this spin valve device along with a fit to a model that includes thermal activation (TA), Mott variable range hopping (VRH),[56] and a linear term for ballistic transport (BT),[57] $1/\rho_{Sheet} = \sigma_{Sheet} = \sigma_{TA} + \sigma_{VRH} + \sigma_{BT}$, where $\sigma_{TA} = A \exp[-E_a/2k_BT]$, $\sigma_{VRH} = B \exp[-(T/T_0)^{1/3}]$, and $\sigma_{BT} = CT$. Fitting parameters are the thermal activation energy $E_a = 0.757$ eV, temperature constant $T_0 = 0.796$ K, and relative conductivities $A = 0.0357$ Ω, $B = 1.88 \times 10^{-4}$ Ω, and $C = 2.03 \times 10^{-4}$ Ω. In the low-temperature regime (T<40 K), the VRH model dominated the temperature-dependent conduction. A stronger thermal activation or a two-state system instead of the variable range hopping was expected in this heterostructure due to the observed temperature-dependent phase change. We attribute the behavior to variable range hopping over the relevant temperature scales; however, the data do deviate from the model at higher temperatures.

Returning to a study of the spin dynamics, Figures 5c,d display the Hanle fit parameters g and τ_s as a function of temperature. Figure 5c shows two average g values; for $T < 40$ K, $g = 0.43 \pm 0.05$, while for $T > 40$ K, $g = 1.8 \pm 0.2$. Higher temperature fits did not converge using the lower temperature g value and vice versa. This is entirely consistent with a Lifshitz phase transition as identified above. Figure 5d shows that the extracted spin lifetime versus temperature also has two regimes. In regime I, the spin lifetime is higher, reaching values as large as 2.18 ns. Above 40 K, it transitions to regime II, where the spin lifetimes are markedly lower, only ≈500 ps. The extracted spin lifetime versus temperature here was for one device, though behavior was similar for all devices tested (additional information is provided in the Supporting Information). Calculated as discussed above, the spin diffusion length $\lambda_s = 13.1$ μm for $\tau_s = 2.18$ ns. In our previous work, electron–electron interactions were used to estimate an effective spin-orbit (SO) interaction of 4.5 meV.[21] Using the values from the Hanle measurement here, an effective SO interaction[58] could also be determined. For the assumed D'yakonov–Perel' spin relaxation mechanism, $\tau_s^{DP} = \hbar^2 / (4\,\Delta_{SO}^2 \tau_q)$, gives $\Delta_{SO} = 0.206$ meV. This value is an order of magnitude lower than the previous estimated interaction, which could be a result of interference between the Rashba and injection/extraction spin channels.

To our knowledge, the highest reported spin lifetime values in literature include gated graphene non-local devices with $\tau_s = 12.2$ ns with an applied gate voltage of $V_G = 70$ V and $\tau_s = 7.7$ ns when $V_G = 0$ V.[59] Values for heterostructures with graphene, e.g., transition-metal-dichalcogenide/graphene heterostructures, have spin lifetimes on the order of 50 ps.[60]

3. Conclusion

In conclusion, we demonstrated high-quality spin transport in a Gr/PST structure along with a temperature-dependent Lifshitz transition. We observed spin-momentum locking in the NLSV measurements due to a giant Rashba SOC, which we further calculated using DFT. Spin transport survives to at least 500 K and the devices display a long spin lifetime, long diffusion length, and high spin polarization efficiency as measured through Hanle effect measurements. The observation of a Lifshitz quantum phase transition in this heterostructure could be incorporated as the switching mechanism in a future ultra-low power computing device. Further, as results of the polar catastrophe are general for any polar/non-polar heterostructure, we predict that additional heterostructures with remarkable spintronic properties using other novel materials are imminently available and should be studied in the future.

Supporting Information

Supporting Information is available from the Wiley Online Library or from the author.

Acknowledgements

The authors gratefully acknowledge support from the Office of the Secretary of Defense in an Applied Research for Advancement of S&T Priorities program (TEDs). The authors gratefully acknowledge technical support assistance at LPS from D. Crouse, P. Davis, R. Brun, G. Latini, and J. Wood. P.D. and I.N acknowledge support by the W. M. Keck Foundation and the NSF Grant number DMR-1752840. P.D. and I.N used the Bridges-2 cluster at PSC through allocation PHY180014 from the Advanced Cyberinfrastructure Coordination Ecosystem: Services & Support (ACCESS) program, which was supported by National Science Foundation Grants Nos. 2138259, 2138286, 2138307, 2137603, and 2138296, and the Maryland Advanced Research Computing Center. D.H. and A.F. thank support from NSF grant DMR-1905662 and the Air Force Office of Scientific Research award FA9550-20-1-0247. The work at the US Naval Research Laboratory was supported under base programs through the Office of Naval Research.

Conflict of Interest

The authors declare no conflict of interest.

Data Availability Statement

The data that support the findings of this study are available from the corresponding author upon reasonable request.

Keywords

2D electron gas, 2D materials, graphene, heterostructure, spin-momentum locking, spintronics, topological materials

Received: September 27, 2023
Revised: October 27, 2023
Published online:

[1] A. K. Geim, I. V. Grigorieva, *Nature* **2013**, *499*, 419.
[2] D. C. Yost, A. L. Friedman, A. T. Hanbicki, J. C. Grossman, *ACS Nano* **2022**, *16*, 9498.
[3] A. T. Hanbicki, H.-J. Chuang, M. R. Rosenberger, C. S. Hellberg, S. V. Sivaram, K. M. Mccreary, I. I. Mazin, B. T. Jonker, *ACS Nano* **2018**, *12*, 4719.
[4] T. Mueller, E. Malic, *npj 2D Mater. Appl.* **2018**, *2*, 29.
[5] Y. Cao, V. Fatemi, S. Fang, K. Watanabe, T. Taniguchi, E. Kaxiras, P. Jarillo-Herrero, *Nature* **2018**, *556*, 43.
[6] J. H. Pixley, E. Y. Andrei, *Science* **2019**, *365*, 543.
[7] P. Wei, S. Lee, F. Lemaitre, L. Pinel, D. Cutaia, W. Cha, F. Katmis, Y.u Zhu, D. Heiman, J. Hone, J. S. Moodera, C.-T. Chen, *Nat. Mater.* **2016**, *15*, 711.
[8] H. Haugen, D. Huertas-Hernando, A. Brataas, *Phys. Rev. B* **2008**, *77*, 115406.
[9] A. Avsar, J. Y. Tan, T. Taychatanapat, J. Balakrishnan, G. K. W. Koon, Y. Yeo, J. Lahiri, A. Carvalho, A. S. Rodin, E. C. T. O'farrell, G. Eda, A. H. Castro Neto, B. Özyilmaz, *Nat. Commun.* **2014**, *5*, 4875.
[10] K. Song, D. Soriano, A. W. Cummings, R. Robles, P. Ordejón, S. Roche, *Nano Lett.* **2018**, *18*, 2033.
[11] M. Gibertini, M. Koperski, A. F. Morpurgo, K. S. Novoselov, *Nat. Nanotechnol.* **2019**, *14*, 408.
[12] M. C. Lemme, D. Akinwande, C. Huyghebaert, C. Stampfer, *Nat. Commun.* **2022**, *13*, 1392.
[13] V. K. Sangwan, H.-S. Lee, H. Bergeron, I. Balla, M. E. Beck, K.-S. Chen, M. C. Hersam, *Nature* **2018**, *554*, 500.
[14] P. M. Solomon, *Annu. Rev. Mater. Sci.* **2000**, *30*, 681.
[15] V. Sverdlov, S. Selberherr, *Phys. Rep.* **2015**, *585*, 1.
[16] W. Han, R. K. Kawakami, M. Gmitra, J. Fabian, *Nat. Nanotechnol.* **2014**, *9*, 794.
[17] G. M. Stephen, A. T. Hanbicki, T. Schumann, J. T. Robinson, M. Goyal, S. Stemmer, A. L. Friedman, *ACS Nano* **2021**, *15*, 5459.
[18] M. Vojta, *Rep. Prog. Phys.* **2003**, *66*, 2069.
[19] R. Okugawa, H. Oshiyama, M. Ohzeki, *Phys. Rev. Res.* **2021**, *3*, 043064.
[20] M. Gmitra, J. Fabian, *Phys. Rev. Lett.* **2017**, *119*, 146401.
[21] G. M. Stephen, I. Naumov, N. A. Blumenschein, Y.-J. Leo Sun, J. E. Demell, S. N. Shirodkar, P. Dev, P. J. Taylor, J. T. Robinson, P. M. Campbell, A. T. Hanbicki, A. L. Friedman, *ACS Nano* **2022**, *16*, 19346.
[22] S.-Y. Xu, C. Liu, N. Alidoust, M. Neupane, D. Qian, I. Belopolski, J. D. Denlinger, Y. J. Wang, H. Lin, L. A. Wray, G. Landolt, B. Slomski, J. H. Dil, A. Marcinkova, E. Morosan, Q. Gibson, R. Sankar, F. C. Chou, R. J. Cava, A. Bansil, M. Z. Hasan, *Nat. Commun.* **2012**, *3*, 1192.
[23] J. T. Robinson, S. W. Schmucker, C. B. Diaconescu, J. P. Long, J. C. Culbertson, T. Ohta, A. L. Friedman, T. E. Beechem, *ACS Nano* **2013**, *7*, 637.
[24] A. L. Friedman, O. M. J. Van T Erve, C. H. Li, J. T. Robinson, B. T. Jonker, *Nat. Commun.* **2014**, *5*, 3161.
[25] B. J. Jönsson-Åkerman, R. Escudero, C. Leighton, S. Kim, I. K. Schuller, D. A. Rabson, *Appl. Phys. Lett.* **2000**, *77*, 1870.
[26] G. Kresse, J. Furthmüller, *Phys. Rev. B* **1996**, *54*, 11169.
[27] G. Kresse, D. Joubert, *Phys. Rev. B* **1999**, *59*, 1758.
[28] J. P. Perdew, K. Burke, M. Ernzerhof, *Phys. Rev. Lett.* **1996**, *77*, 3865.
[29] P. E. Blöchl, *Phys. Rev. B* **1994**, *50*, 17953.
[30] A. Ambrosetti, A. M. Reilly, R. A. Distasio, A. Tkatchenko, *J. Chem. Phys.* **2014**, *140*, 18A508.
[31] X. Lou, C. Adelmann, S. A. Crooker, E. S. Garlid, J. Zhang, K. S. M. Reddy, S. D. Flexner, C. J. Palmstrøm, P. A. Crowell, *Nat. Phys.* **2007**, *3*, 197.
[32] D. D. Hiep, M. Tanaka, P. N. Hai, *Appl. Phys. Lett.* **2016**, *109*, 232402.
[33] O. M. J. Van T Erve, A. T. Hanbicki, M. Holub, C. H. Li, C. Awo-Affouda, P. E. Thompson, B. T. Jonker, *Appl. Phys. Lett.* **2007**, *91*, 212109.
[34] S. Jafarpisheh, F. Volmer, Z. Wang, B. Canto, Y. Ando, C. Stampfer, B. Beschoten, Non-local electrical detection of spin-momentum-locked surface currents in the 3D topological insulator BiSbTeSe2. Preprint at, https://doi.org/10.48550/arXiv.1907.10347, **2019**.
[35] H. J. Kim, M. S. Katsiotis, S. Alhassan, I. Zafiropoulou, M. Pissas, Y. Sanakis, G. Mitrikas, N. Panopoulos, N. Boukos, V. Tzitzios, M. Fardis, J.-G. Kim, S.-G. Lee, Y.-M. Kim, S. J. Yoo, J.-H. Lee, A. Kouloumpis, D. Gournis, M. Karakassides, G. Papavassiliou, *NPG Asia Mater* **2016**, *8*, e271.
[36] A. Manchon, H. C. Koo, J. Nitta, S. M. Frolov, R. A. Duine, *Nat. Mater.* **2015**, *14*, 871.
[37] R. H. Silsbee, *Phys. Rev. B* **2001**, *63*, 155305.
[38] J. Nitta, T. Akazaki, H. Takayanagi, T. Enoki, *Phys. Rev. Lett.* **1997**, *78*, 1335.
[39] T. H. Hsieh, H. Lin, J. Liu, W. Duan, A. Bansil, L. Fu, *Nat. Commun.* **2012**, *3*, 982.
[40] K. Ishizaka, M. S. Bahramy, H. Murakawa, M. Sakano, T. Shimojima, T. Sonobe, K. Koizumi, S. Shin, H. Miyahara, A. Kimura, K. Miyamoto, T. Okuda, H. Namatame, M. Taniguchi, R. Arita, N. Nagaosa, K. Kobayashi, Y. Murakami, R. Kumai, Y. Kaneko, Y. Onose, Y. Tokura, *Nat. Mater.* **2011**, *10*, 521.
[41] Y. Xia, D. Qian, D. Hsieh, L. Wray, A. Pal, H. Lin, A. Bansil, D. Grauer, Y. S. Hor, R. J. Cava, M. Z. Hasan, *Nat. Phys.* **2009**, *5*, 398.
[42] T. Nishimura, H. Sakai, H. Mori, K. Akiba, H. Usui, M. Ochi, K. Kuroki, A. Miyake, M. Tokunaga, Y. Uwatoko, K. Katayama, H. Murakawa, N. Hanasaki, *Phys. Rev. Lett.* **2019**, *122*, 226601.
[43] N. C. Bristowe, P. Ghosez, P. B. Littlewood, E. Artacho, *J. Phys. Condens. Matter* **2014**, *26*, 143201.
[44] S. Hong, V. Diep, S. Datta, Y. P. Chen, *Phys. Rev. B* **2012**, *86*, 085131.
[45] C. H. Li, O. M. J. Van T Erve, S. Rajput, L. Li, B. T. Jonker, *Nat. Commun.* **2016**, *7*, 13518.
[46] C. H. Li, O. M. J. Van T Erve, C. Yan, L. Li, B. T. Jonker, *Sci. Rep.* **2018**, *8*, 10265.
[47] P. R. Hammar, B. R. Bennett, M. J. Yang, M. Johnson, *Phys. Rev. Lett.* **1999**, *83*, 203.
[48] J. S. Moodera, J. Nassar, G. Mathon, *Annu. Rev. Mater. Sci.* **1999**, *29*, 381.
[49] S. Sayed, S. Hong, X. Huang, L. Caretta, A. S. Everhardt, R. Ramesh, S. Salahuddin, S. Datta, *Phys. Rev. Appl.* **2021**, *15*, 054004.
[50] R. H. Silsbee, *J. Phys. Condens. Matter* **2004**, *16*, R179.
[51] I. Zutic, J. Fabian, S. Das Sarma, *Rev. Mod. Phys.* **2004**, *76*, 323.
[52] N. Menezes, V. S. Alves, E. C. Marino, L. Nascimento, L. O. Nascimento, C. Morais Smith, *Phys. Rev. B* **2017**, *95*, 245138.
[53] R. L. Hota, G. S. Tripathi, *J. Phys. Condens. Matter* **1991**, *3*, 6299.
[54] K. Výborný, G. Mihajlovic, A. Hoffmann, S. I. Erlingsson, *J. Phys. Condens. Matter* **2013**, *25*, 216007.

[55] O. Maksimov, X. Zhou, M. C. Tamargo, N. Samarth, *Phys. E* **2006**, *32*, 399.
[56] A. L. Friedman, C. D. Cress, S. W. Schmucker, J. T. Robinson, O. M. J. Van T Erve, *Phys. Rev. B* **2016**, *93*, 161409.
[57] M. Müller, M. Bräuninger, B. Trauzettel, *Phys. Rev. Lett.* **2009**, *103*, 196801.
[58] A. L. Friedman, K. M. Mccreary, J. T. Robinson, O. M. J. Van T Erve, B. T. Jonker, *Carbon* **2018**, *131*, 18.
[59] M. Drögeler, C. Franzen, F. Volmer, T. Pohlmann, L. Banszerus, M. Wolter, K. Watanabe, T. Taniguchi, C. Stampfer, B. Beschoten, *Nano Lett.* **2016**, *16*, 3533.
[60] T. S. Ghiasi, J. Ingla-Aynes, A. A. Kaverzin, B. J. van Wees, *Nano Lett.* **2017**, *17*, 7528.

